Effective de-icing skin using graphene-based flexible heater

L. Vertuccio[a*], F. De Santis[a,c], R. Pantani[a], K. Lafdi[b], L. Guadagno[a**]

[a] Department of Industrial Engineering, University of Salerno, Via Giovanni Paolo II, Fisciano (SA) Italy

[b] University of Dayton, 300 College Park, Dayton, OH, United States

[c] Borealis Polyolefine GmbH, Innovation Headquarters, St. Peterstr. 25, 4021 Linz, Austria

*lvertuccio@unisa.it; fedesantis@unisa.it; rpantani@unisa.it; klafdi1@udayton.edu, **lguadagno@unisa.it

Abstract

In this study, a thermal de-icing/anti-icing system for aircraft surfaces was designed using flexible graphene film/paper. It was placed between two Carbon Fiber Reinforced Plastic (CFRP) laminates. The flexible heater paper presents high mechanical and thermal properties and requires up to nine times less power than current known resistance heating pad thermal systems to achieve de-icing. The temperature of the surface was controlled by varying the power input. This allows the monitoring of de-icing time, which can be tuned in less than 10 minutes. The feasibility of the de-icing performance was demonstrated through a series of experiments and the results indicate that the developed method could be a very promising electrical heating strategy able to maintain lightness, efficiency in the de-icing performance and for reducing the environmental impact of de-icing realized through polluting fluids.

Keywords:

Carbon-carbon composites (CCCs)

Smart materials

De-icing

Expanded graphite

1. Introduction

The de-icing of an aircraft is crucial when there are freezing conditions and precipitation. Frozen contaminants cause critical control surfaces to be rough and uneven, disrupting smooth air flow and greatly reducing the ability of the wing to generate lift, and increasing drag. This situation can cause a serious safety risk to the aircraft, and thus to the pilots and the passengers. Frozen contaminants can jam control surfaces, preventing them from moving properly. Because of this potentially severe consequence, de-icing is performed at airports where temperatures are likely to be around or

below 0°C. Wing ice management falls into two broad categories: anti-icing (ice prevention) and de-icing (ice elimination or mitigation). Most technology focuses on de-icing, operating on the assumption that some ice is going to form on a wing and works to get it off before it becomes problematic. Almost all de-icing technologies rely on a substance (usually a sprayable chemical applied prior to take-off) or an onboard mechanism that destabilizes the ice, thus allowing the slipstream to dislodge it and remove it from the wing. In particular, the aircraft is armed with different icing protection systems: 1) active systems, which require an energy input; 2) passive systems, which do not require energy, such as surface treatments. Several approaches have been used to provide de-ice and/or anti-ice systems for modern aircraft and these are also categorized as mechanical, chemical or thermal. Mechanical methods involve breaking ice formations off protected structures. They require the deformation of the underlying surface to produce enough strain to break the ice-surface bond. An inflatable elastomeric membrane, known as a "boot," is one of the most common mechanical de-icing systems [1]. Its effectiveness is reliant on the pilot's ability to see the condition of ice on the wing, which is not always trivial in harsh weather. Chemical icing protection is centered on lowering the freezing point of water. Glycol fluid is used for ground de-icing because it is relatively low cost, and its viscosity at low temperatures allows for a thin film of the fluid to remain on the aircraft for some time before take-off. The thin film is generally removed after take-off by strong convection as the aircraft reaches its rotation speed [1]. A typical thermal system, limited to turbine aircraft, diverts bleed air or hot air from one of the turbine stages to heat the airfoil leading edges [2]. Other thermal systems employ electrically conducting resistance heating elements, such as those contained in heating pads bonded to the leading edges of the aircraft or on the propeller or rotor blades, or those incorporated into the structural members of the aircraft. Heating pads of this type usually consist of an electrically conductive material in contact with the wire or other metal heating elements dispersed throughout the conductive layer, which is sandwiched, between two insulation layers. Electrical energy for the heating elements is derived from a generating source driven by one or more of the aircraft engines [2]. The electrical energy is continuously supplied to provide heat sufficient to prevent the formation of ice or intermittently supplied to release the accumulating ice. However, such systems could be only adopted where sufficient wattage is available to raise and/or maintain the temperature of the airfoil surface above the freezing point at typical aircraft speeds. For example, an anti-ice system that is continuously on during icing conditions should ideally maintain a surface temperature of approximately 38°C to 54°C, i.e. as required in the Gulfstream Pilot Operating Handbook [3]. To achieve such temperatures, the required power supply for anti-icing or de-icing system could be high [4, 5]. Specifically, a typical general aviation light aircraft with an approximate anti-icing area of 0.90 m^2, using pad heaters, requires approximately 23250 W/m^2 to reach anti-ice temperatures. Known heating pad systems supply only 3100 W/m^2 to 4650 W/m^2 at the power supplied by these aircrafts. In recent years, a number of alternative systems have been proposed, which attempt to improve the power efficiency and operational effectiveness of

anti-icing or de-icing systems. Different novel materials have been investigated as the heating element, including an electro-conductive textile [6], carbon nanotubes (CNTs) [7], sprayable metal layer [8], carbon fibers (CF) [9] and constantan wires [10]. Furthermore, CNTs have been used for preparing CNT-webs (horizontally oriented continuous films, obtained by drawing CNT forests produced by carbon vapour deposition), which were utilized as electro-thermal heating element for anti-icing and de-icing of composite structures [11]. Very promising results were obtained in terms of weight, and level of uniformity achieved in the temperature of the assembled structural parts. In another case, a perfluorododecylated graphene nanoribbon (FDO-GNR) film has been designed. The film has proven to have integrated advantages of both the low polarizability of perfluorinated carbons and the intrinsic conductive nature of graphene nanoribbons[12]. The new strategies above mentioned, based on carbon nanostructured forms, seem to be very promising to impart efficient anti/de-icing properties to structural components. On the other hand, the use of conductive polymers for this specific application, despite their advantage of lightness, results difficult due to low thermal conductivities and poor mechanical performance. Many current polymeric materials show shortages in practical applications on structural surfaces because of their poor resistance to shear stress, low strength, high brittleness and the difficulty of being malleable for surface covering. An alternative approach consisting of 2D conductive paper can satisfy the requirements for surface engineering with the coupling compliance, structural compatibility, and flexibility after mechanical encapsulated protection and reinforcement by multi-layered structures. Currently, the use of graphite or graphite derivatives for production of heating papers can address the requirements described above. The structures of graphite derivatives papers are designed by controlling stacking processes and assembling orientations of the multilayers; therefore, these materials can bear relatively large deformations with outstanding flexibility and mechanical robustness [13]. Currently, 2D graphite derivatives films can be directly fabricated by chemical vapor deposition process [14], oxide paper reduction [15, 16], directly aqueous dispersion [17], electrophoretic deposition [18], and roll-to-roll producing strategy [19].

However, the intrinsic brittleness for anti-shear force among graphite sheet in nanoscale and thin thickness induced low strength make them difficult to defeat large tensile strain, which severely restrains their widespread applications as conductive Joule heating unless the structural encapsulation and mechanical reinforcement are sufficiently implemented. In this work, expanded graphite, readily commercially available material and relatively inexpensive, is used to produce a flexible expanded graphite foil with the introduction of PVA, by an easy and green solvent casting process.

The combination of polymer and expanded graphite allows obtaining a flexible exfoliated graphite film/paper, well suited, in terms of surface area to volume, for conducting heat and electricity. The required wattage for producing a rapid rise in temperature in different environmental temperature conditions is far less than that required by known

electrical wire heating systems. The developed strategy provides a de-icing and anti-icing system for aircraft that can be an integral part of the aeronautical panels and hence of the aircraft structure. In this sense, experimental tests considering a Carbon Fiber Reinforced Plastics (CFRP) assembled system, were carried out, in view of the fact that the use of composites, in the aircraft field, has significantly increased in the past few decades; not without reason, the Boeing and Airbus, have placed on the market the 787 and A350 airbuses respectively, where the presence of composite material exceeds 50% of the airframe. This investigation allowed to evaluate the de-icing and ice-melting performance in drastic environmental conditions (-32°C).

The flexible film/paper, bonded between flexible insulating layers, provides a laminate that is easy to die cut, to size and configure to a variety of aircraft structural shapes, including control sur-faces and other irregularly shaped removable and movable components.

2. Experimental

2.1 Materials and methods

2.1.1 Preparation of Exfoliated graphite

Exfoliated graphite (EG) was prepared from a natural flake graphite provided by Superior Graphite. It is characterized by the following parameters: Carbon purity % = 98.6, Size 1"×8 mesh, Bulk Density (g/100 mL) = 17.80, Sulfur (%) = 0.056 and Resistivity (Ωcm) = 0.0316. Starting with natural graphite with an average diameter of 500 μm, the EG was prepared as follows: a mixture, containing nitric and sulphuric acid (volume ratio = 135 ml / 255 ml) and natural graphite, was prepared. After 24 h of reaction, intercalation within graphene sheets took place to form intercalated graphite. Then the mixture was filtered, washed with water, and dried in an oven at low temperatures. The intercalated graphite compound was subjected to sudden heat treatment temperature of 900°C and rapid expansion then occurred. Changes in the degree of exfoliation were obtained by varying the resident time in the fluidized bed as the time increases, the trapped intercalate and/or gases would have a second chance to escape causing further expansion and exfoliation.

2.1.2 Preparation of Carbon Fiber Reinforced Panels

The carbon fiber reinforced panels used in this work was obtained following a well-defined procedure described in previous papers [20, 21]. Fiber-reinforced composite parts were cut into flat coupons 5×5 cm^2 with a nominal thickness of 1.15 mm. A diamond tip water-cooled saw blade was used to this purpose.

2.1.3 Preparation of the film/paper and the assembled composite

A synthetic scheme illustrating the sequence of the steps for the preparation the heater conductive flexible film is shown in Fig.1. The exfoliated graphite (Fig. 1a) was suspended and mixed by magnetic stirring in a solution of deionized water and PVA having a ratio PVA/water (g/ml) of about 0.3 g in 75 ml in order to obtain a good solubilization of the polymer in water. As soon as the magnetic stirring finished, the exfoliated graphite floated onto the surface of the solution (Fig. 1b). Two-hour ultra-sonication process has proven to improve the dispersion of graphite nano-sheets in the liquid mixture allowing to obtain a stable EG solution (Fig. 1c). Afterwards, a 200 μm-thick flexible film/paper (Fig. 1d) was obtained by evaporation casting, followed by thermal annealing at 120°C for 1 h applying a pressure of 500 psi. A ratio by weight of exfoliated graphite /PVA equal to 60/40 has been chosen in order to obtain on the one hand high electrical conductivity (> 1000 S/m), on the other hand a satisfying film flexibility. The subsequent stages related to the preparation of the Carbon Fiber Reinforced Composite (CFRC) integrating the conductive flexible heater paper to obtain a part of the final anti-icing/de-icing aeronautical structure is shown in Fig.2. In particular, a film/paper of the dimensions 5 cm x 5 cm has been used. Two Cu foils strips, acting as electrodes, with a thickness of 80 mm were adhered on both sides of film/paper (see Figure 2a), in order to apply a suitable electric current density and hence evaluate the heating temperature by the use of thermocouples appositely placed on both surfaces of the film /paper (see Figure 2a). The anti/de-icing reinforced epoxy composite was assembled by embedding the flexible film/paper, with the Cu foil contacts and the thermocouples, between two CFRP laminates with a thickness of 1.15 mm each, by the use of two 0.130 mm-thick epoxy-based adhesive films as shown in the scheme of Figure 2b. The adhesive film was supplied by Sigma Aldrich (trade name: FM® 73 Epoxy Film Adhesive).
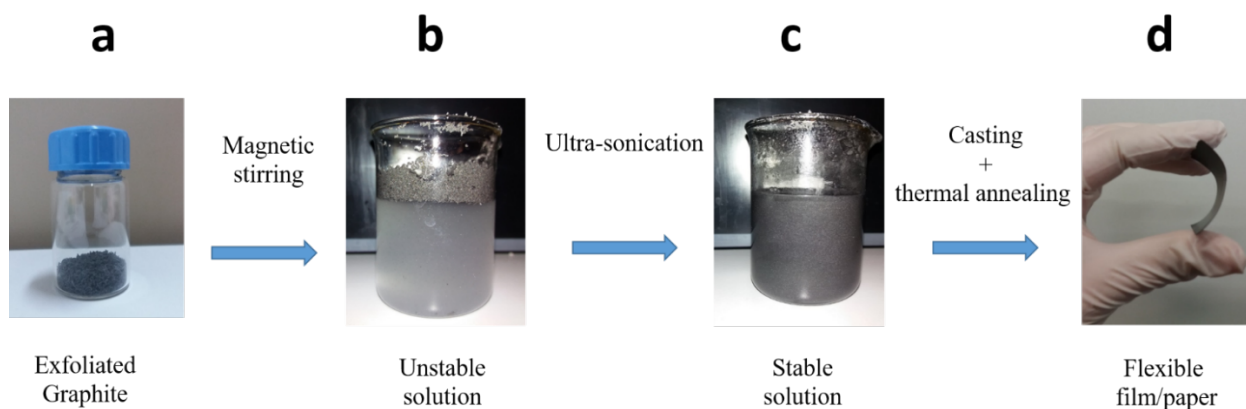
Fig. 1. Illustration of the fabrication process of the film/paper.
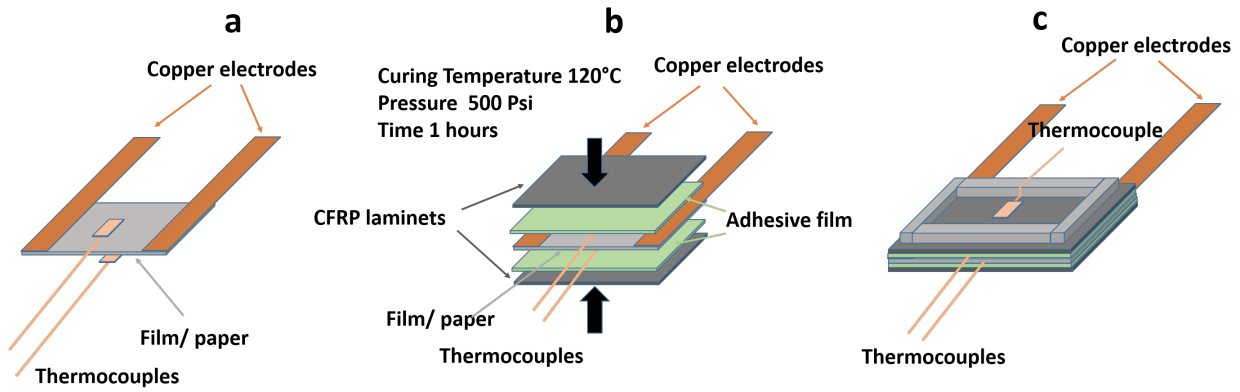
Fig. 2. Schematic illustration of the fabrication processes of assembled composite: a) schematic of electrodes and thermocouples configuration adopted; b) schematic process of the assembled composite; c) ultimate configuration of the system.

The assembled system was treated at 120°C for 1 h with a pressure of about 500 psi, to allow a strong adhesion of the adhesive film between the laminates. Subsequently, another thermocouple was placed on the upper surface of the assembled composite for the monitoring of the temperature on surface of the assembled piece and for evaluating the de-icing phenomenon. In order to confine the ice and the water on the surface of the assembled composite, a square with an inner side of 4.2 cm and a height of 1 cm was realized and bonded on the surface of the composite (see Figure 2c). Water, with a volume of 10 ml, was used for a formation of ice, resulting in a thickness of about 0.6 cm.

2.2 Characterization methods

2.2.1 Structural Analysis

X-ray diffraction analysis, in combination with SEM investigation, was used to evaluate the exfoliation degree of the expanded graphite employed for the preparation of the heater conductive flexible film shown in fig. 1d. Wide-angle X-ray diffraction (WAXD) pattern was obtained by an automatic Bruker D8 Advance diffractometer operating at 35 kV and 40 mA. The nickel filtered Cu-Kα radiation (1.5418 Å) was used.

2.2.2 Morphological Analysis

Scanning electron microscope **(**SEM) micrographs of exfoliated graphite and the heater conductive flexible film were obtained with a field emission Scanning Electron Microscopy (SEM) apparatus (JSM-6700F, JEOL) instrument

operating at 3 kV. The exfoliated graphite was analyzed as prepared (without further treatment), whereas the flexible film was etched before the SEM investigation. In particular, some of the film/paper sections were cut from the solid samples by a sliding microtome. The slices were etched using an etching reagent, which was prepared by stirring 1.0 g potassium permanganate in a solution mixture of 95 mL sulphuric acid (95–97%) and 48 mL orthophosphoric acid (85%). The slice of film/paper was immersed in the fresh etching reagent at room temperature and held under agitation for 1 hours. Subsequent washings were done using a cold mixture of 2 parts by volume of concentrated sulphuric acid and 7 parts of water. Afterward, the samples were washed again with 30% aqueous hydrogen peroxide to remove any manganese dioxide. The samples were finally washed with distilled water and kept under vacuum for 5 days. This experimental procedure has proven to be very effective to better analyze the morphological feature of nanocomposites [22, 23].

2.2.3 Spectroscopic Analysis

Raman spectra were obtained at room temperature with a micro-Raman spectrometer Renishaw inVia with a 514 nm excitation wavelength (laser power 30 mW) in the range (400–3000 cm^{-1}). In order to separate the individual peaks in the case of unresolved, multicomponent bands, a curve resolving algorithm was applied, based on the Levenberg–Marquardt method [24]; to reduce the number of adjustable parameters and to ensure the uniqueness of the result, the baseline, the band shape and the number of components were fixed. The minimum number of components was evaluated by visual in the section based on abrupt changes of slope of the experimental line-shape. The program was then allowed to calculate, by a non-linear curve fitting of data, the height, the full-width half height (FWHH) and the position of the individual components. The peak function was a mixed Gauss–Lorentz line shape of the form [25]:

$$f(x) = (1-L)H \exp\left[-4\ln(2)\left(\frac{x-x_0}{w}\right)^2\right] + LH\left[4\left(\frac{x-x_0}{w}\right)^2 + 1\right]^{-1} \tag{1}$$

where x_0 = the peak position; H = peak height; w = FWHH; L = fraction of Lorentz character. FTIR spectra were obtained at a resolution of 2.0 cm^{-1} with a FTIR (BRUKER Vertex70) spectrometer equipped with deuterated triglycine sulfate detector and a KBr beam splitter, using KBr pellets. The frequency scale was internally calibrated to 0.01 cm^{-1} using a He-Ne laser. 32 signal scans were averaged to reduce the noise.

2.2.4 Evaluation of Mechanical Properties

Dynamic mechanical properties of the samples were performed with a dynamic mechanical thermo-analyzer (Tritec 2000 DMA-Triton Technology). The samples with dimensions 0.2×10×15 mm^3 were tested by applying a variable

tensile deformation. The displacement amplitude was set to 0.03 mm, whereas the measurements were performed at the frequency of 1 Hz. The range of temperature was from -60°C to 180°C at the scanning rate of 3°C min^{-1}.

2.2.5 Evaluation of Thermal Properties

Thermogravimetric analysis (TGA) was carried out in air using a Mettler TGA/SDTA 851 thermal analyzer. The temperature range was 30-1000°C at a heating rate of 10°C min^{-1}.

Differential Scanning Calorimetry (DSC) was carried out on sample using a thermal analyzer Mettler DSC 822/400 (Mettler-Toledo) equipped with DSC cell purged with nitrogen and chilled with liquid nitrogen for sub-ambient measurements. Temperature range was -60-300°C at a heating rate of 10°C min^{-1}. Calorimetric traces were utilized for evaluate the melting analyzed samples.

2.2.6 Electrical conductivity and temperature measurement

In order to characterize the electrical resistance of the samples, a 4-wire method was used, using an HP 34401A Digital Multimeter. A data acquisition board (DAQ NI-USB 6210 supplied by the National Instruments) was used to acquire the thermocouples measurements. In order to record the local temperature evolution, a dedicated LabView software was developed. The temperatures were measured using thin wire thermocouples (Type T, about 100 μm of diameter supplied by Omega Engineering Ltd.) with a negligible thermal inertia, which were positioned at the center of flexible heater paper. The laboratory power supply EA-PS 2042-20B (Elektro-Automatik, 0-42 V, 0-10 A, 320 W max) was connected to the heater paper, as described in the following section, remotely controlled and monitored by the LabView software. All measurements were performed in direct current (DC) mode, with a selected constant current. The temperature distribution was measured by a thermal infrared (IR) Camera (Fluke Ti 100).

3. Results and discussion

3.1 Structural and morphological analysis

3.1.1 Structural and morphological analysis of the exfoliated graphite

X-ray pattern of the exfoliated graphite is shown in Figure 3. The intense and narrow 002 reflection, characteristic of graphite-based particles, appears superimposed on a broad amorphous halo. The ratio between the area of the 002 peak and of the amorphous halo roughly centered at about $2\theta = 26°$ (see red curve of the Figure 3) allows to evaluate the percentage of exfoliated graphite considering that for a sample of completely exfoliated graphite, no reflections of

crystalline phases are observed. This hypothesis is not only confirmed by a theoretical point of view, but also by many

structural investigations carried out on different samples of graphene based samples [26] . Under this hypothesis, the

percentage of exfoliated phase was assumed as the percentage of the amorphous phase (X_a), whereas the percentage of

the graphitic phase was assumed as the percentage of the crystalline phase (X_c). This assumption is very plausible also

in light of the morphological results which prove that, no amorphous phase different from exfoliated graphite is

observable in the sample EG. X_a and X_c were calculated applying a standard procedure of resolving the diffraction

pattern into two areas, A_c and A_a, in the range of 2θ between $15°-40°$, using the Equation 2

$$X_c = 100 \frac{A_C}{A_c + A_a} \tag{2}$$

according to the classical Hermans–Weidinger method [27]. Appling this method, the percentage of exfoliated graphite

(X_a) in the EG sample resulted of 53%.
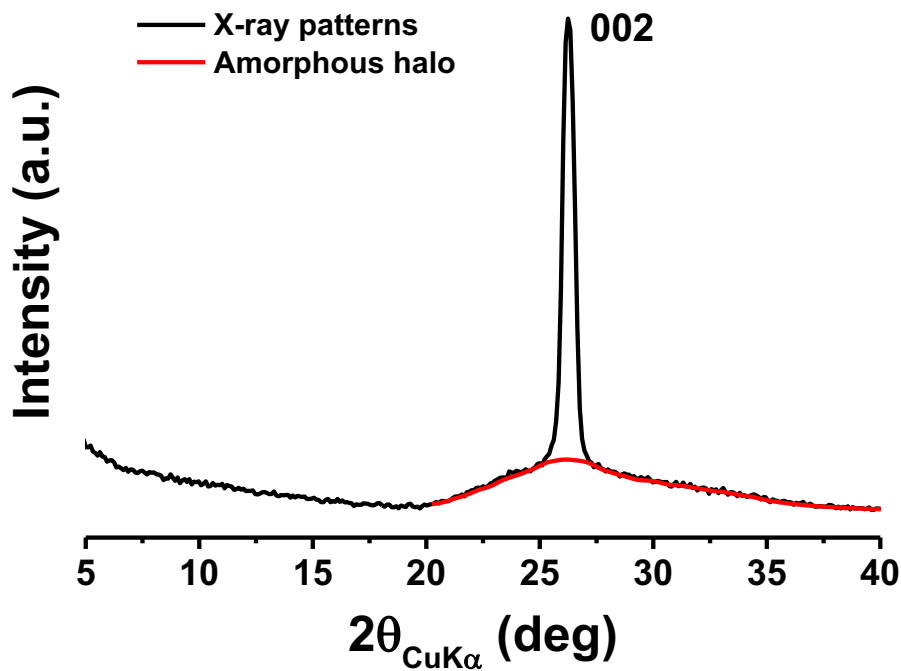
Fig. 3. X ray diffraction of Exfoliated graphite.

From Scherrer's equation [28], the average in the number of layers can be obtained using the following equation [29]:

$$Number\ of\ layers = \frac{D_{002}}{d_{002}} \tag{3}$$

where D_{002} is the crystallite coherence length perpendicular to the reflection plane 002. Considering the value of 3.39 Å for the d-spacing of the reflection (002), a number of about 35 layers has been calculated for graphitic block of EG sample.

SEM micrographs of the as-prepared exfoliated graphite (before the preparation of the solution of Fig. 1b) are shown in Fig. 4.
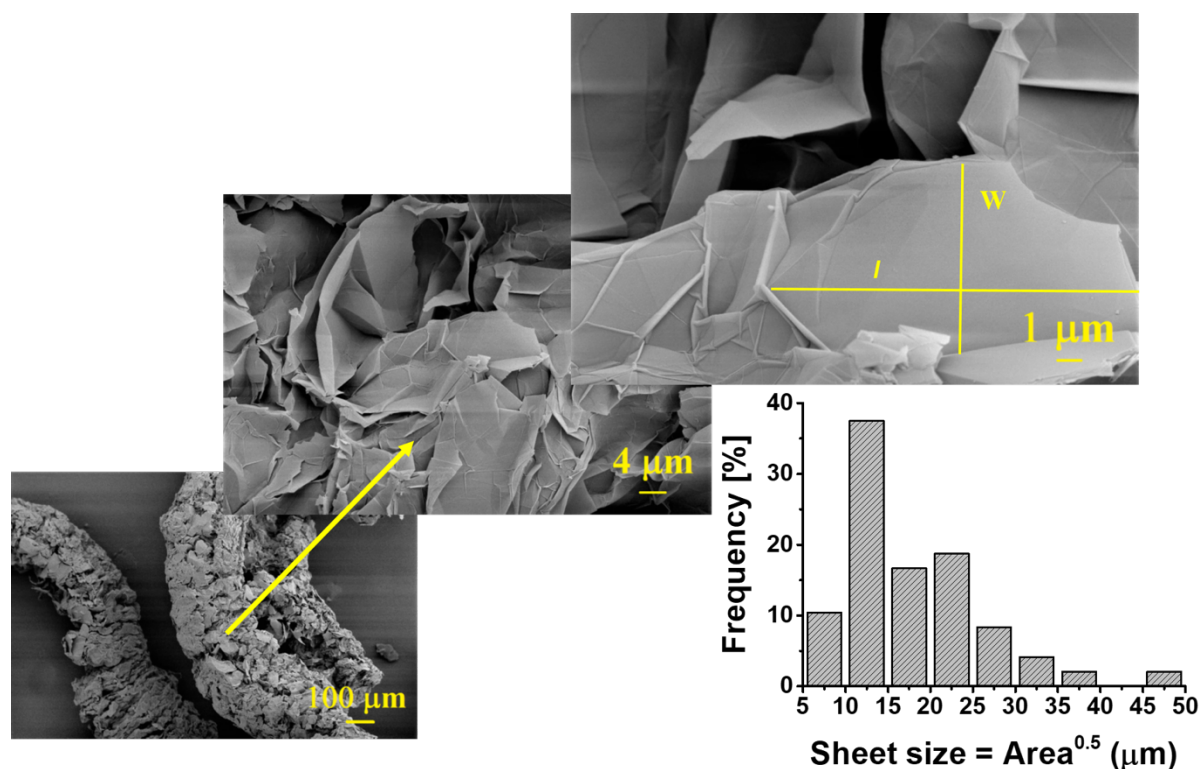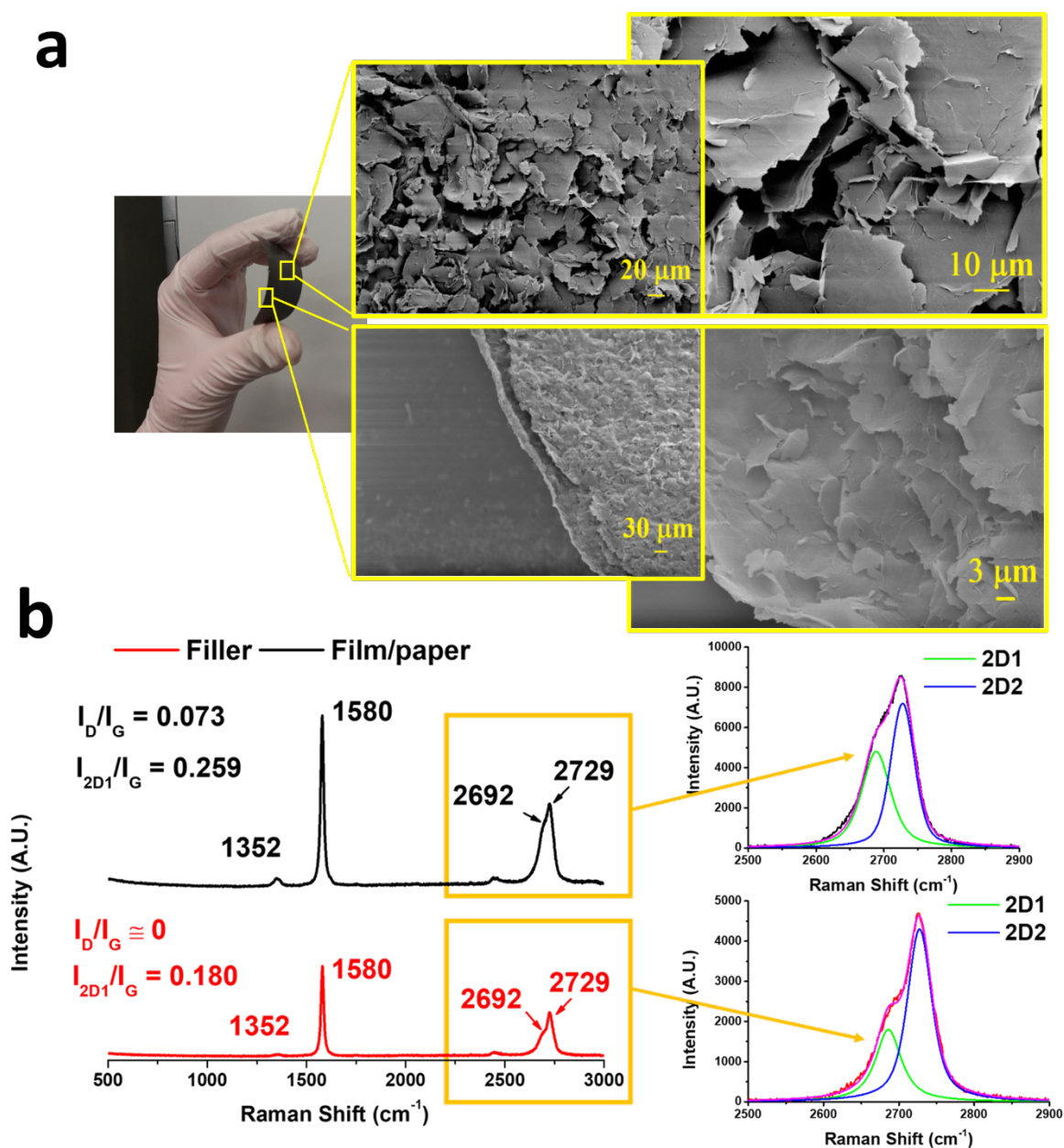

Fig. 4. SEM images of the pristine exfoliated graphite and histogram distribution of the sheets size obtained measuring the area of each sheet.

The as-prepared exfoliated graphite nanoparticles appear like worm-like or accordion structure. At higher magnifications, as seen in the picture, the nanosheets of the exfoliated graphite can be clearly observed. If, on one hand, a porous-like structure with very straight and polygonal graphene walls not separated is observed, on the other hand many hole-like spaces between the nanosheets are observed, which are most likely caused by the greatly expanded volume. It is well known in the literature that 2D nanosheets from exfoliated graphite have highly irregular shapes; therefore, a detailed investigation of the geometrical parameters of the 2D nanosheets was performed to calculate the size of the sheets. The calculation was performed using an advanced software for the image analysis (Sigma SCAN-Analyze Image Automatically), as follow: for each sheet, two geometrical parameters were measured, the length l, measured along the longer segment and the maximal width W measured in the direction perpendicular to the length l

(see Figure 4). For regular rectangular sheets, the area was simply calculated as the product of l and W. This type of calculation is not accurate for irregular shapes such as those typically obtained by the exfoliation of graphitic materials. In particular, to obtain a reliable parameter, not depending on a particular shape, the square root of the sheet area was calculated: $s = \sqrt{area}$. In the case of regular rectangular shapes, this would be simply $s = \sqrt{lW}$; for irregular sheets, this has the same dimensionality but is a more reliable parameter than the length l. Different from l, s does not depend on the sheet shape, but only on the exact area. This calculation procedure has already been applied by other authors [30]. Statistical analysis was performed through one-by-one localization of the dimensions of the sheet in the SEM images, by the use of the above-mentioned software. Several SEM images were analyzed in order to acquire dimensions on a number of 100 sheets. The use of the software Origin (OriginLab) allowed the evaluation of the distribution of the size of the analyzed sheets. Figure 4 shows the distribution of the sheet size, it highlights that the distribution is quite large, ranging between 7.5μm and 47.5 μm. However, a prevalence of the frequency around the value of 10-25 μm is observable, confirming that the thermal expansion during the exfoliation process, causes a strong reduction in the size of the sheets initially characterized by an average diameter of 500 μm.

3.1.2 Structural and morphological analysis of the flexible conductive film

The exfoliated graphite was used for preparing the flexible film/paper, which was characterized by SEM analysis and Raman spectroscopy. Figure 5 shows the SEM images and the Raman spectra of the film/paper prepared as described in the Experimental section.


Fig. 5. Microstructural characterizations of the film/paper: a) SEM images of the film/paper; b) Raman spectra of the exfoliated graphite and the film/paper.

In order to evaluate the stacking conditions of the exfoliated graphite sheets embedded in the flexible film, SEM analysis was carried out both on the surface of the paper and along the cross-section of the paper (see Figure 5a). Along the surface of the paper, the exfoliated graphite sheets are only partially stacked; in other areas, instead, the sheets appear like folded structures. However, most of the sheets tend to be arranged parallel to the film plane. Along the cross section, the exfoliated graphite appears more corrugated and as a highly packaged structure. The corrugated structure is most likely due the presence of capillary stress induced by a slight shrinkage during water evaporation [31] and during the annealing stage, as already found for similar samples by other authors [31]. In any case, from the observed SEM images, at different magnifications, a tissue/like structure is observed; the exfoliated graphite seems uniformly assembled layer-by-layer in the cross-section of the paper. Strong π- π interactions among graphene nanoplates efficaciously facilitate the good connection of ordered inter-junctions and portend a surpassing combination of mechanical robustness and electrical conductivity, as proved by the results related to the mechanical and electrical measurements discussed in the next section. The peculiar nature of the developed film promises many relevant applications in many fields of science and nanotechnology, including flexible electrodes, stimuli-responsive sensors, and Joule heating skins. In addition to the SEM investigation, the state of the exfoliated graphite within the film/paper was evaluated by Raman spectroscopy. The Micro-Raman (MR) spectra of the exfoliated graphite and the film/paper is shown in Fig. 5b. For both the sample, the two most intense peaks are the G peak at 1580 cm^{-1} and the peak at about 2700 cm^{-1} known in literature as "2D band"[26, 32]. The G peak is doubly degenerate Raman active optical vibration E_{2g} mode [33],while the 2D band is the second order of zone-boundary phonons. These phonons generate the band at 1352 cm^{-1}, associated with the edge distortion [34]. This last peak is negligibly weak in both spectra of Fig. 5b due to the presence of graphitic blocks in the filler and in the film/paper. The ratio of the D-band (1352 cm^{-1}) to G-band (1580 cm^{-1}) intensities (I_D/I_G) is ~ 0 and around 0.073 for the filler and the film/paper respectively. This ratio can be used to evaluate the level of disorder in graphene. Generally, as disorder in graphene increases, I_D/I_G displays two different behaviors. There is a regime of "low" defect density where I_D/I_G will increase as a higher defect density creates more elastic scattering. This occurs up to a regime of "high" defect density, at which point I_D/I_G will begin to decrease as an increasing defect density results in a more amorphous carbon structure [35]. The film/paper falls within the low-defect-density regime, hence the slightly higher value of I_D/I_G indicates a small increase in the exfoliation degree occurs in the film/paper. The 2D peak between 2600 and 2800 cm^{-1} in bulk graphite consists of two components 2D1 and 2D2 [32]. The relative intensity of these two peaks can be associated with the number of layers of graphene blocks containing less than 5 layers. In particular, an increase in layers leads to a significant decrease of the relative intensity of the lower frequency 2D1 peak [36]. Although the filler and film/paper samples contain graphitic blocks composed of a number of layers > 5, this type of investigation was qualitatively applied to get further information from the MR spectra. In order

to separate the individual peaks 2D1 and 2D2, a curve-resolving algorithm was applied; the ratio I_{2D1}/I_G is 0.180 and 0.259 for the filler and film/paper respectively. The increase in the value of this ratio suggests an increase in the fraction of the exfoliated phase in the film/paper with respect to the filler [26], most likely due to further separation of the thick graphitic layers during the ultrasonication step of the film/paper preparation process.

FTIR spectra of exfoliated graphite are very useful to understand the changes caused by the exfoliation process on graphitic materials. A previous study performed by FTIR investigation on exfoliated graphite at different exfoliation degree and graphene layers (completely exfoliated graphite) highlighted that the exfoliation process determines the formation of oxygenated functional groups (carboxyl, hydroxyl etc.)[26]. This functional groups act as spacers and are able to prevent the reassembly process of the graphene layers (to contrast the Vander Waals attractive forces) in graphitic block during the processing steps. This is a desired condition to better confer the graphene properties to the film/paper.

The FTIR spectrum of the film/paper is shown in Fig. 6, where the spectra of exfoliated graphite (black spectrum) and of a PVA pure reference sample (blue spectrum), obtained in the same condition process of the film/paper, have also been shown for comparison.
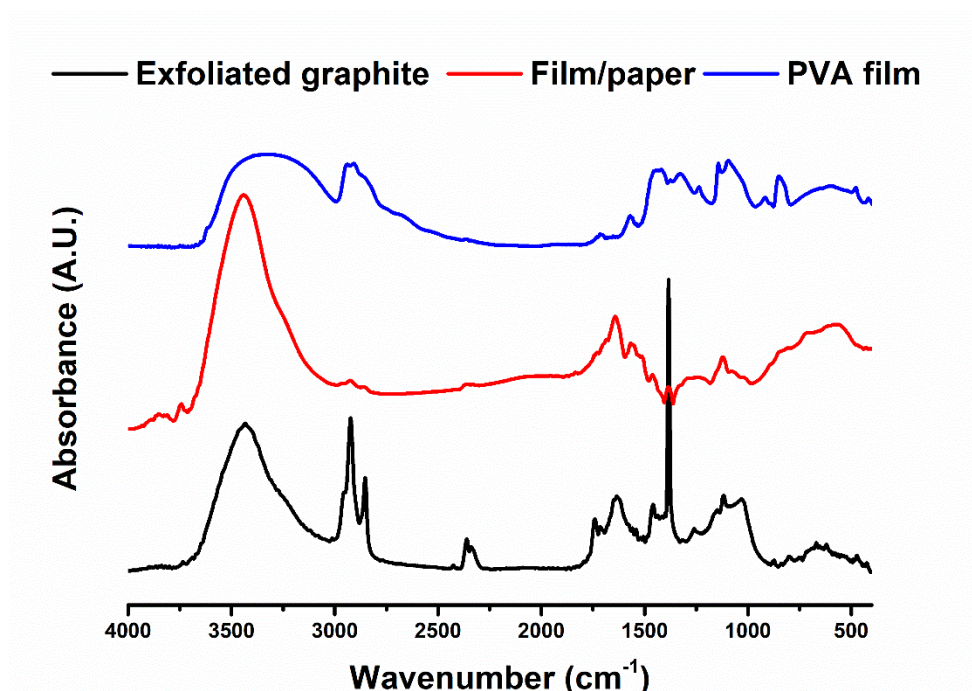
**Fig. 6.** FTIR spectra of the filler, PVA film and the film/paper.

The FTIR spectrum of the PVA clearly reveals the characteristic bands of poly(vinyl alcohol). In particular, bands between 2850 cm^{-1} and 3000 cm^{-1} typical of C–H alkyl stretching and the strong hydroxyl bands for free -OH groups (no bonded –OH stretching peak at ν = 3600–3650 cm^{-1}), and hydrogen bonded band (ν = 3200–3570 cm^{-1}) are

observed. Considering the profiles of the OH signals (3000 – 3700 cm^{-1}) of all samples, the absorption bands at 3280, the OH stretching vibration from intra-/inter-molecular hydrogen bonded hydroxyl groups, seem to be more intense in the spectrum of PVA. In the spectrum of the film/paper, the presence of exfoliated graphite seems to slightly reduce the amount of intra-/inter-molecular hydrogen bonded hydroxyl groups. The signal of -OH free groups in the film paper seems to be more intense than the bonded hydroxyl groups, as also occurs in the spectrum of the exfoliated graphite. The presence of OH free groups makes the film able to create hydrogen bonding interactions with the epoxy laminates or other polar groups of different substrates. The similarity in the spectrum of exfoliated graphite and the film/paper is also due to the low amount of PVA in the film paper.

A comparison between the spectra of the film/paper and that of the exfoliated graphite shows that many signals are attributable to the exfoliated graphite. The absorption bands at 3445 cm^{-1} at 1122 cm^{-1} and 1030 cm^{-1} corresponding to O–H, to C-OH and C–O stretching vibrations, respectively, while the absorption peaks at 1565 cm^{-1} and 1644 cm^{-1} are ascribed to the skeletal vibrations of C=C [37]. In particular, the most intense signals in the range between 1500 cm^1 and 1800 cm^{-1} is the peak at 1644 cm^{-1} due to the graphitic material. The last results highlight that EG consists of oxidized graphite sheets with their basal planes decorated mostly with hydroxyl groups, in addition to carbonyl groups. These oxygen functionalities make the graphite layers hydrophilic, so that water molecules can readily intercalate into the inter-layer galleries. Aqueous PVA solution is a colloidal suspension, wherein the hydroxyl groups become ready acceptors for hydrogen bonding, which increases its interaction with the water molecules, making PVA soluble in water. Hydroxyl groups of PVA, as deduced by the FTIR spectrum, can also form strong hydrogen bonds with oxygenated functional groups present on EG, thereby forming hydrogen-bonded crosslinks between the PVA molecules [38, 39]. Probably the sonication process favors the creation of the interactions just mentioned as it can be seen from Figure 1c, in which the solution based on PVA and EG remains stable even after 24 h. The relative flexibility of the prepared paper/film, (see Figure 5a) is probably due to the amount of folded structures, obtained during the ultra-sonication process, which leads to a greater exfoliation of the graphite.

3.2 Physical analysis of the film/paper

In order to evaluate the thermal stability of graphene film/paper, dynamic mechanical analysis and thermal analysis were performed. Fig. 7 shows: a) the plots of the storage modulus (E') and tan δ of the film/paper as a function of the temperature in the range -60 °C - 180°C (Fig. 7a); b) the thermogravimetric curves of the filler and film/paper as a function of the temperature (Fig. 7b); c) the DSC curve of the film/paper in the temperature range -60 °C ÷ 300°C (Fig. 7 c) and d) the trend in the temperature values of the film/paper, due to Joule heating, as a function of the time (Fig. 7d).
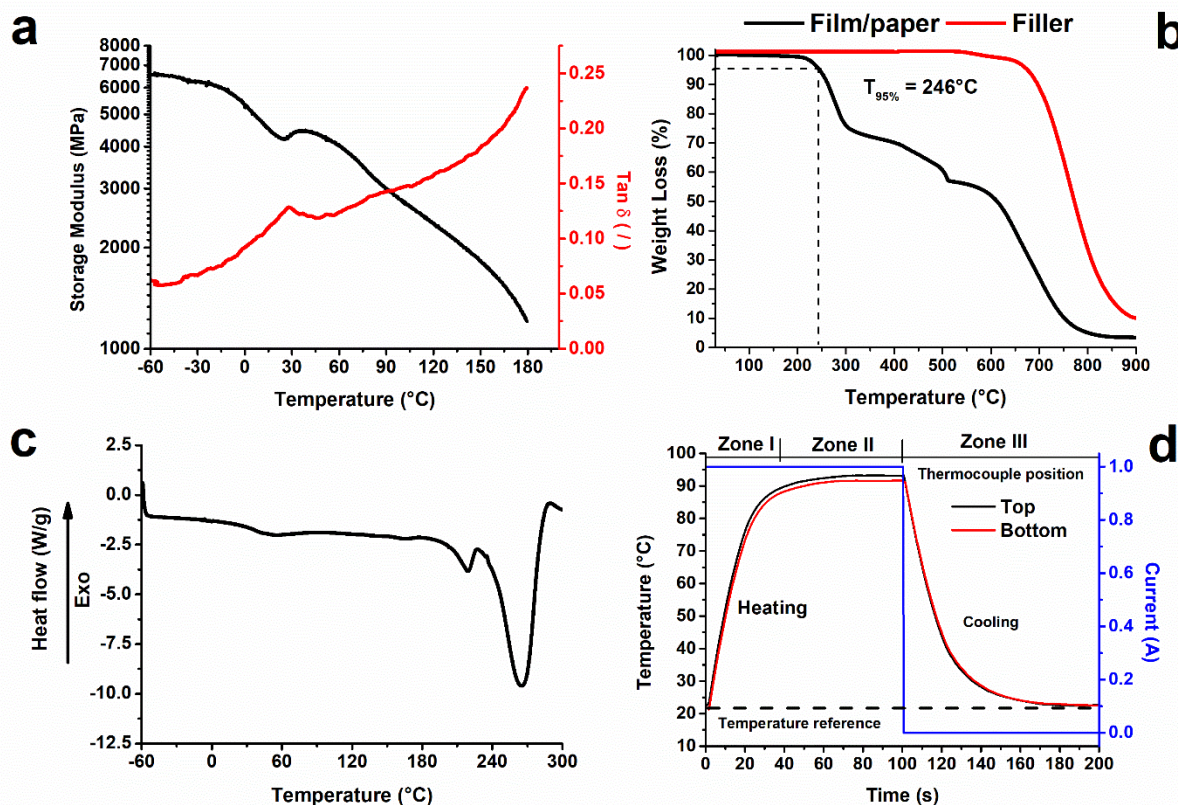
Fig. 7. Physical analysis of the film/paper: a) Dynamic mechanical analysis; b) Thermogravimetric analysis; c) Differential Scanning Calorimetry; d) Temperature vs time during power on-off.

Fig 7a highlights that the storage modulus of the graphene film/paper is higher than 2000 MPa in a very wide temperature range of -60 °C-120°C. The profile of the curve related to the storage modulus shows a slow and progressive decrease of modulus up to 30°C, followed by a slight increase and a second constant drop up to 180°C. The first drop, before the slight increase, ends at 28 ° C, which is the value of the glass transition temperature T_g of the PVA component of the film, as evident by the profile of the curve related to tanδ, which shows the main peak around 30°C. The dynamic mechanical parameters demonstrate an optimized performance. Graphene film/paper shows a high flexibility due to the relatively low glass transition temperature (~28 °C), high storage modulus, especially below 0°C for which values higher than 5000 MPa are detected. Figure 7b shows that, as expected, graphene film/paper degrades before the pure filler. In fact, the first two degradation steps are ascribed to PVA component of the film [40], while the degradation step from 500°C to 700°C is ascribed to exfoliated graphite. The onset-degradation temperature (5% weight-loss temperature) of the graphene film/paper is 246°C. Indeed, graphene film is thermally stable up to 240°C. At higher temperatures, just before the thermal degradation mechanisms, the PVA component melts, as shown in the DSC thermogram of Figure 7c, where the endothermic peak, centered around 264 °C, which corresponds to the melting

temperature of PVA films is observed. The small endothermic peak before the main endotherm is most likely due to melting and partial recrystallization of tiny PVA crystals trapped between graphene and graphitic layers.

The electrical conductivity of graphene film was measured using four-wire technique and the value 6.6×10^3 S/m was obtained. The graphene film temperature profile, due to Joule heating, was recorded as a function of time for different applied electric powers. Each series of measurements was carried out at constant current. An example of the electric heating behavior of graphene film is shown in Figure 7d (for current of 1 A), where the reference temperature was 22°C. All measurements were performed in ambient air in order to have similar boundary conditions on both surfaces of the film/heater. The temperature increases rapidly in the first stage (zone I) with a nearly linear trend to reach a steady state temperature (zone II) in which the temperature achieves an equilibrium value. When the power was turned off, the temperature decreased to a reference temperature (zone III). Furthermore, it is worth noting that the temperature trend on both surfaces is very similar, sometimes overlapping, both in the zone I and in the zone III. A slight difference is observed in the zone II corresponding to the equilibrium temperature. This difference is less than 2°C. Similar differences were obtained at various powers. For this reason, only thermocouple data located at the upper surface of graphene film are shown. In order to analyze the joule heating, at temperature condition below 0°C, the temperature trend, of graphene film, was recorded as a function of time for different applied electric powers at -32°C.

3.3 Electric heating characteristic of graphene film/paper

The results related to the electric heating characteristic of the graphene film/paper are reported in Fig. 8. The relationship between time and temperature for different heat flux densities at 22°C and -32°C is shown in Figs. 8a and 8b respectively. An enlargement of the first zone of fig. 8b, corresponding to the rectangular area highlighted with black perimeter, highlighting only temperatures equal to or less than 5 °C, is shown in Fig. 8d.
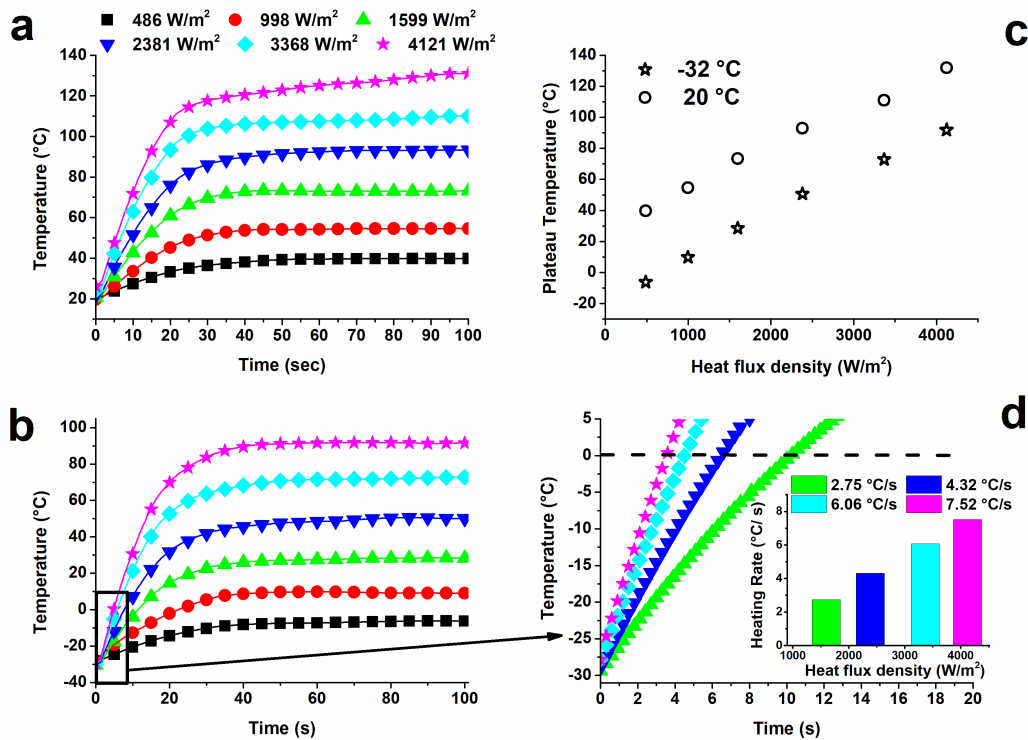
Fig. 8. The Relationship between time and temperature at different heat flux densities for the film/paper at the environmental temperature of 22°C (a), of -32°C (b); the relationship between heat flux densities and the equilibrium temperatures at the two analyzed environmental temperatures of 22 °C and – 32 °C (c); enlargement of the first zone of Fig. 8b corresponding to the rectangular area highlighted with the black perimeter (d).

In particular, data shown in Figs. 8a and 8b were collected starting from two different temperatures of -30°C and 22°C, under different current from 0.4 A to 1.4 A (interval is 0.2 A) corresponding to heat flux densities of 486, 998, 1599, 2381, 3368 and 4121 W/m^2 respectively. From the plots, it is clear that the surface temperature firstly rapidly increases and then reaches a plateau corresponding to the equilibrium temperatures on the surface of the sample. The equilibrium temperature of the sample increases gradually as the heat flux density increases and the time required for reaching the equilibrium temperature becomes gradually longer. At the beginning, the temperature dramatically increases rapidly

because of the high conductivity properties of graphene film. According to Figures 8a and 8b, it is obvious that the

equilibrium temperature increases gradually at different heat flux densities, while the heating rate accelerates with the

heat flux densities increasing from 456 to 4121 W/m^2. The high heating rate means that the graphene film/paper is

suitable for de-icing because, in general, electrical heating materials for de-icing are required to reach a high

temperature in a short time period. For all curves of Figs. 8a and b, a linear trend is observed in the initial part. The

range of linearity is dependent on the heat flux density. As an instance, considering the environmental temperature of -

32°C for heat flux densities higher than 1599W/ m^2, the temperature trend vs. time is linear at least up to a surface

temperature of 5° C (Fig 8d). In those conditions, it is possible to define a real heating rate, from the slope of the

corresponding curves. As described before, in Figure 8d, the heating rate is shown for different heat flux densities and

can be evaluated up to a temperature range of 5°C higher than the freezing temperature of 0°C (that goes from 0°C to

5°C), a condition for which the de-icing phenomenon occurs. The rate was found very high, from a minimum of

2.75°C/s for a heat flux density of 1599 W/m^2 to a maximum of 7.52°C/s for a heat flux density of 4121 W/m^2. In any

case, the temperature of 0°C was reached in 10 seconds. Figure 8b reveals that the environmental temperature

influences the equilibrium temperature. For each given heat flux density, the equilibrium temperature approximately

increases of about 40-45°C. This last temperature gap is almost equivalent to the difference between the two

environmental temperatures of -32°C and 22°C. In order to verify and to confirm that the obtained graphene film/paper

can be an alternative to known resistance heating pad thermal systems, below, a comparison between a silicone rubber

wire heater and the graphene film/paper is shown (see Table 1).

Table 1. Comparison between a silicone rubber wire heater (SRWH)[3] and graphene film/paper (F/P)

Sample	Environmental Temperature (°C)	Heat flux density (W/m^2)	Power* (W)	Temperature achieved (°C)	Time to achieve the temperature (34°C) (s)	Temperature achieved in 90 sec. (°C)
F/P	-32	2548	132	34	38	54
F/P	-32	3689	190	34	12	76
F/P	-32	4542	234	34	10	91
SRWH	-0.5	23250	1233	34.4	90	34.4

*Applied power for a surface area of 0.052 m^2

A comparison was done considering a surface of 0.052 m^2, in which the silicone rubber wire heater requires 1233 W or

23250W/m^2[1], to raise the temperature of the surface from -0.5°C to 34.4°C in 90 s. As illustrated in Table 1,

considering the heat flux densities from 2548 W/m^2 to 4542 W/m^2, the power generated by the graphene film/paper

ranges from 132 W to 234 W. This is 5 to 9 times lower than the power generated by current wire heating pad systems

proposed for aircraft. It is important to note that this evaluation was made considering environmental starting

conditions. In particular, the evaluation for the graphene film/paper was done in the more drastic temperature of -32°C, not -0.5°C, which is the environmental temperature of the tests performed on the silicone rubber wire heater. Despite these drastic conditions compared to those considered for a standard current wire heating pad system (-0.5 °C), with a power of 234 W, the temperature of 34 °C is reached within 10 seconds, whereas for SRWH, with a power of 1233 W, the temperature of 34.4 °C is reached in 90 seconds. An estimate of the film weight in terms of the ratio weight/area has been made; if a 50 μm thick film is considered, the ratio weight/area is about 35 g/m^2, which is among the lower values reported in literature for other heating systems. Concerning this last point, the results of a very complete and accurate investigation have been reported by Yao et al.[11]. These authors have developed highly aligned CNT-web-heater, which possesses negligible weight; they have been compared the obtained results with the already existing systems or other systems described in literature. Even if, the system described in this paper is different from all the reported systems, the comparison highlights the great applicative potential of the strategy here described. Infrared images of the film/paper have been collected during joule heating process in order to evaluate the heating uniformity of the electro-thermal film.
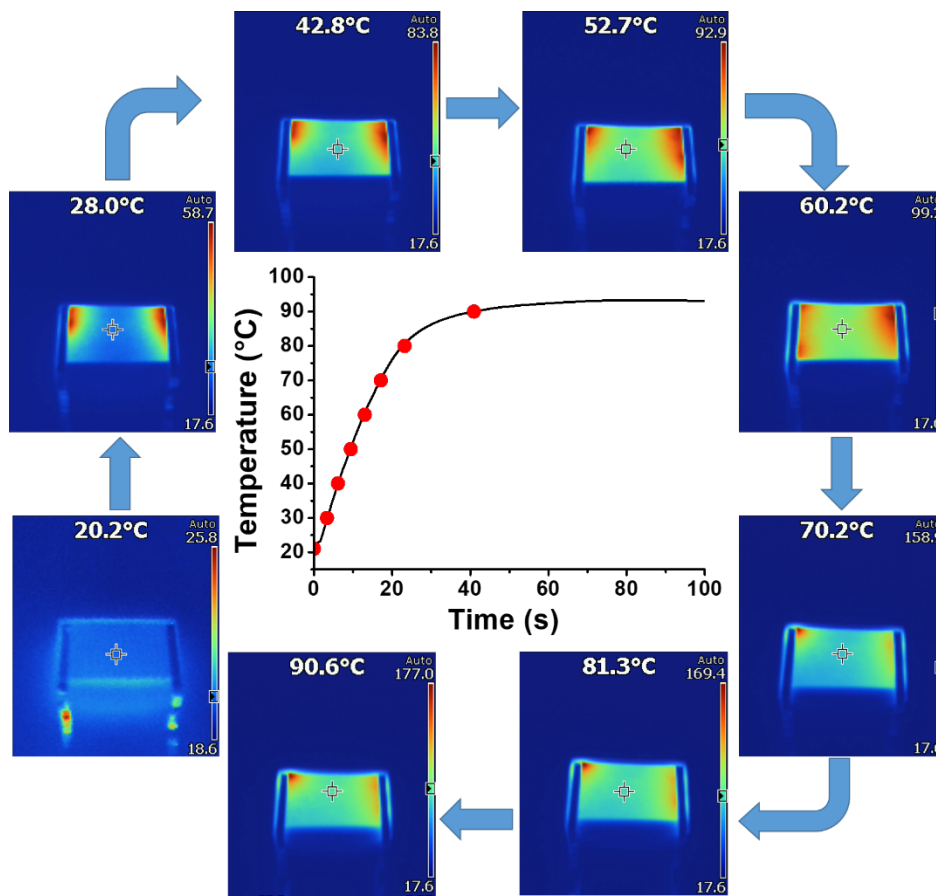

Fig. 9. Infrared images of the film/paper during joule heating process.

In particular, in Figure 9, the temperature profile of a film/paper (dimensions 8 cm x 4 cm) vs time during heating has been monitored applying a current of 1A. The results show that the temperature distribution of the film/paper becomes more and more uniform as the temperature approaches that of the plateau value. However, for all temperatures, an almost homogeneous temperature distribution is detected. In fact, the area characterized by uniform colour is never less than 70/80% of the entire surface. The temperature uniformity found is most likely due to the uniform thickness of the sample and a satisfying homogeneity in the nanofiller distribution.

3.4 Electric heating characteristic of assembled composite

It is very interesting to investigate the film/paper's Joule temperature performance to evaluate its real potentiality as an effective de-icing strategy. To perform these tests, an assembled composite system was used (Figure 2c). The results of the heating and de-icing procedure are shown in Figure 10. The reference temperature was -32°C. Figure 10 shows the temperature profile as a function of time. An endoscopic camera was inserted in the freezer in order to visually monitor the de-icing process.
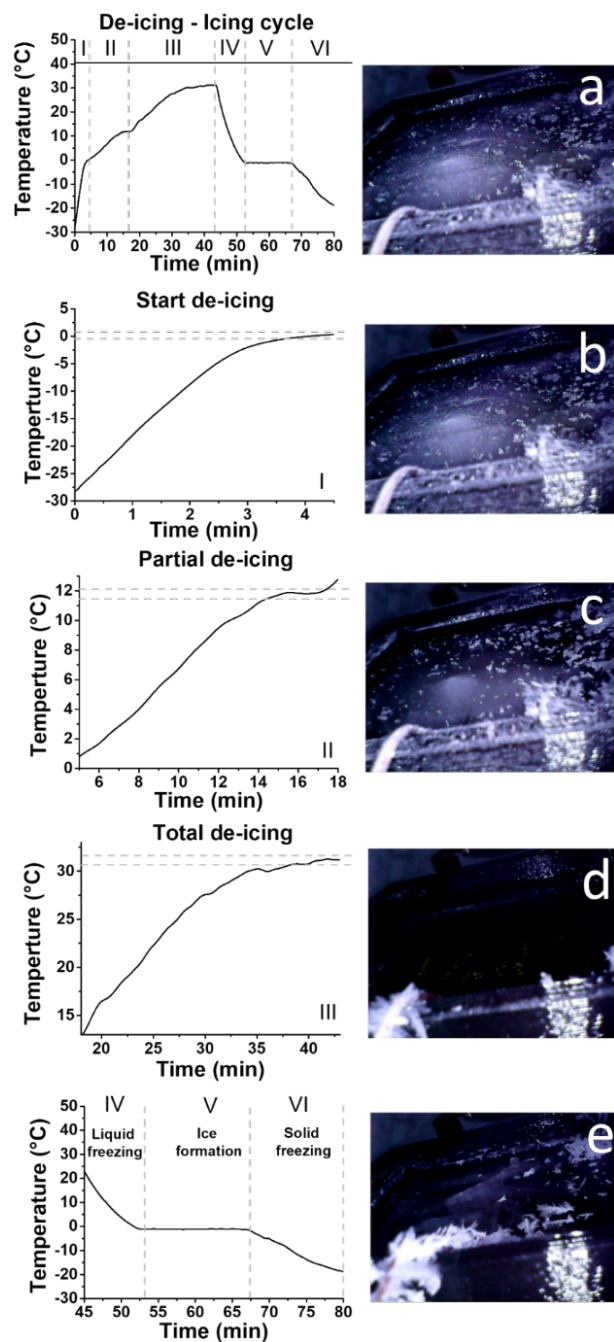
Fig. 10. Temperature vs time during power on-off of the assembled composite at the environmental temperature of -32°C, with evaluation of de-icing process (heat flux density 3706 W/m^2) by an endoscopic camera.

As soon as power was supplied, the temperature increased rapidly in a first stage (zone I) with a linear trend to reach a plateau temperature of 0°C, at which de-icing starts. The enlargement of the first stage (zone I) is shown in Fig. 10b. The temperature remained constant at 0°C for one minute and then increased again (Figure 10c). At this point the first layer of ice, which was in contact with the composite, melted, while the rest of the ice remained solid, as shown in Figure 10c. In zone II and III, the temperature increased at a lower rate. An image micrograph was taken at end of the zone II, in which it can be observed that the amount of ice decreased. At end of the zone III, all the ice melted. Zones IV, V, VI are related to liquid freezing, ice formation (Figure 10e) and solid freezing, respectively. Figure 11 shows the temperature profile as a function of time, obtained by thermocouples positioned on both the graphene film/paper surfaces.
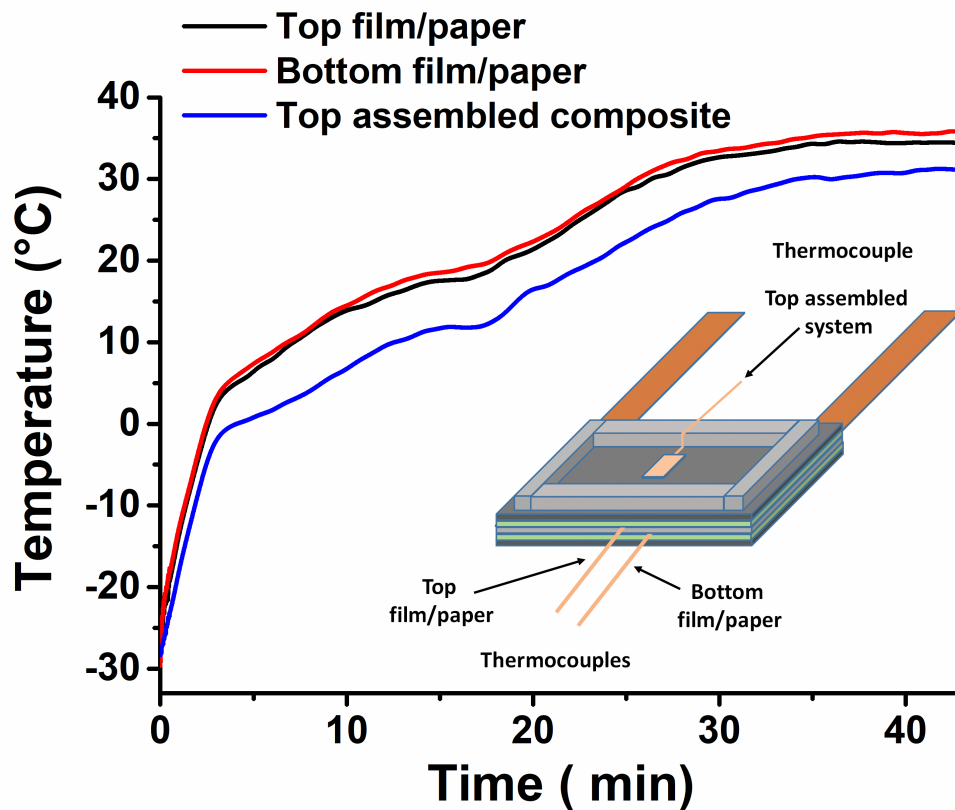
Fig. 11. The temperature profile as a function of time during the power on stage of the assembled composite, at environmental temperature of -32°C, during the de-icing process, for all used thermocouples (heat flux density 3706 W/m^2).

As shown, in Fig. 11, there is almost an overlap of the profiles in the zone I, while in the other zones there was temperature difference of about 5°C. These results demonstrate that, within the range of electric powers used, the inside of the assembled system was not subjected to excessive heat, which may compromise the integrity of the graphene

film/paper (T<180°C). The effect of the increasing heat flux densities (1741, 3706, 2634, 5831 W/m²) on de-icing for the assembled composite is shown in Figure 12.
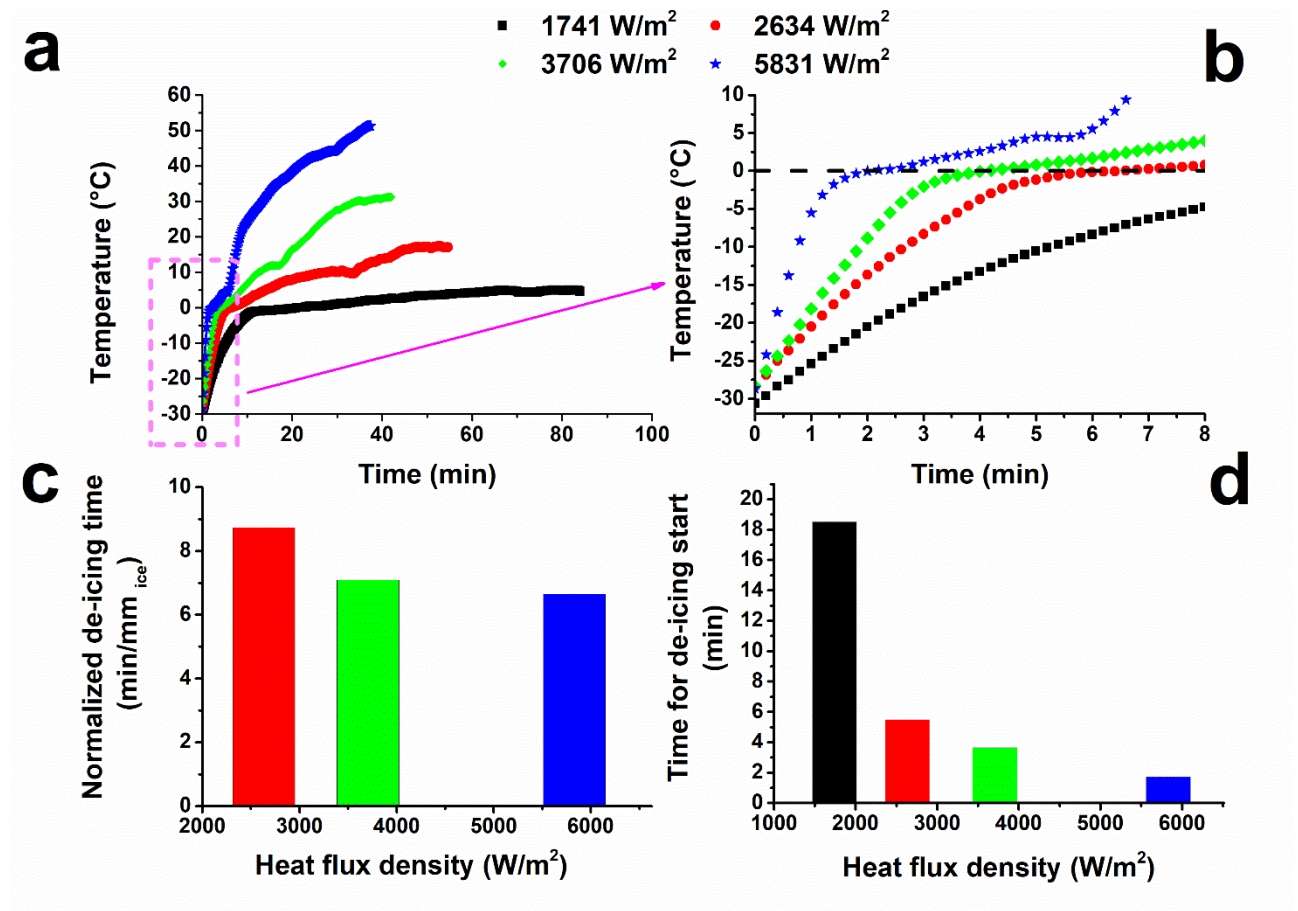
Fig. 12. a) The relationship between time and temperature at different heat flux densities for the assembled composite during the de-icing process; b) increase in the temperature range from -32°C to 10°C; comparison of the normalized de-icing time at different heat flux densities; d) comparison of the response times of the assembled composite at different heat flux densities.

To achieve effective de-icing, for the considered geometry (see section 2.1.3) at least 1741 W/m² is required. In fact, with this value of heat flux density (see black curve in Fig. 12a), the system reaches the temperature of 0°C only after 18 min, and then the temperature reaches the plateau value around 7°C, which is not sufficient to completely melt the ice in a short period of time. Higher values of heat flux density result in a complete melting of the ice, making possible both a reduction of the de-icing time (Figure 12c) and the time to achieve the defrizzing temperature of 0°C (see 12b,12d). Considering the value of the highest heat flux density used in this work, starting with the environmental temperature of -32°C, it is possible to melt a 1 mm-thick layer of ice in less than 9 minutes. In future work, in order to increase the response speed of the de-icing assembled composite, the possibility of positioning the graphene film/paper

directly on the surface of the composite will be considered. Overall, the response times of the system are very low even in the worst conditions, which correspond to an environmental temperature of -32°C; whereas usually the de-icing systems currently used are activated when the environmental temperature drops down to just below 0 °C.

4. Conclusions

There is a high demand for the improvement of de-icing technology in aeronautics. Ideal technology must be reliable, inexpensive, must require low power and be light.

In this study, an attempt was made to fulfill this portfolio. For this reason, a flexible lightweight heater foil, based on exfoliated graphite, was integrated into composite aeronautical panels. The flexible resistive heater graphene film/paper exhibits an electrical conductivity of 6.6×10^3 S/m and a storage modulus of over 2000 MPa that can operate in the temperature range from -60°C to 120°C. The flexibility of the graphene film is due to the low value of the T_g related to the PVA component (28 °C) and the folded structure of the most exfoliated graphite (combination of graphene layers and thin graphitic layers). The surface of the graphene layers is functionalized with different oxygen groups. The combination between surface chemistry and the physical properties of the graphene films make this heater an effective current ideal de-icing material.

The test results show that this carbon heater is very efficient and highly competitive to the current resistive heater. The temperature of the surface of the graphene film can be easily controlled by varying the power input. The proposed strategy may constitute a significant progress towards implementation of energy-saving structures in the aircraft transport field. The developed system can also work with lower power consumption. Considering the value of the highest heat flux density and the environmental temperature of -32°C, it is possible to melt a 1 mm-thick layer of ice in less than 7 min. The feasibility of the de-icing performance was demonstrated through a series of experiments and the results indicate that the developed method could be a very promising electrical heating strategy able to maintain lightness and efficiency in the de-icing performance and for reducing the environmental impact of de-icing currently realized through polluting fluids.

References

[1] Heinrich A, Ross R, Zumwalt G, Provorse J, Padmanabhan V. Aircraft Icing Handbook. Volume 2. GATES LEARJET CORP WICHITA KS; 1991.

[2] Parent O, Ilinca A. Anti-icing and de-icing techniques for wind turbines: Critical review. Cold Reg Sci Technol 2011;65(1):88-96.

[3] Rutherford RB. De-ice and anti-ice system and method for aircraft surfaces. Google Patents; 2001.

[4] Buschhorn ST, Kessler SS, Lachmann N, Gavin J, Thomas G, Wardle BL. Electrothermal icing protection of aerosurfaces using conductive polymer nanocomposites. 54th AIAA/ASME/ASCE/AHS/ASC Structures, Structural Dynamics, and Materials Conference2013. p. 1729.

[5] Strehlow RH, Moser R. Capitalizing on the increased flexibility that comes from high power density electrothermal deicing. SAE Technical Paper; 2009.

[6] Falzon BG, Robinson P, Frenz S, Gilbert B. Development and evaluation of a novel integrated anti-icing/de-icing technology for carbon fibre composite aerostructures using an electro-conductive textile. Composites Part A 2015;68:323-35.

[7] Brampton CJ, Bowen CR, Buschhorn ST, Lee J, Pickering SG, Wardle BL, et al. Actuation of bistable laminates by conductive polymer nanocomposites for use in thermal-mechanical aerosurface de-icing systems. 55th AIAA/ASMe/ASCE/AHS/SC Structures, Structural Dynamics, and Materials Conference2014. p. 0105.

[8] Sloan J. 787 integrates new composite wing deicing system. High Performance Composites. 2009;17(1):27-9.

[9] Li CL, Cui X, Wu ZH, Zeng JC, Xing SL. A method of eliminating ice on wind turbine blade by using carbon fiber composites. Adv Mater Res: Trans Tech Publ; 2013. p. 1322-5.

[10] Mohseni M, Amirfazli A. A novel electro-thermal anti-icing system for fiber-reinforced polymer composite airfoils. Cold Reg Sci Technol 2013;87:47-58.

[11] Yao X, Hawkins SC, Falzon BG. An advanced anti-icing/de-icing system utilizing highly aligned carbon nanotube webs. Carbon 2018;136:130-8.

[12] Wang T, Zheng Y, Raji A-RO, Li Y, Sikkema WK, Tour JM. Passive anti-icing and active deicing films. ACS Appl Mater Interfaces 2016;8(22):14169-73.

[13] Davami K, Zhao L, Lu E, Cortes J, Lin C, Lilley DE, et al. Ultralight shape-recovering plate mechanical metamaterials. Nat Commun 2015;6:10019.

[14] Kim KS, Zhao Y, Jang H, Lee SY, Kim JM, Kim KS, et al. Large-scale pattern growth of graphene films for stretchable transparent electrodes. Nature 2009;457(7230):706.

[15] Dikin DA, Stankovich S, Zimney EJ, Piner RD, Dommett GH, Evmenenko G, et al. Preparation and characterization of graphene oxide paper. Nature 2007;448(7152):457.

[16] Šimek P, Sofer Z, Jankovský O, Sedmidubský D, Pumera M. Oxygen-Free Highly Conductive Graphene Papers. Adv Funct Mater 2014;24(31):4878-85.

[17] Chen H, Müller MB, Gilmore KJ, Wallace GG, Li D. Mechanically strong, electrically conductive, and biocompatible graphene paper. Adv Mater 2008;20(18):3557-61.

[18] Yao Y, Fu KK, Yan C, Dai J, Chen Y, Wang Y, et al. Three-dimensional printable high-temperature and high-rate heaters. ACS Nano 2016;10(5):5272-9.

[19] Bae S, Kim H, Lee Y, Xu X, Park J-S, Zheng Y, et al. Roll-to-roll production of 30-inch graphene films for transparent electrodes. Nature Nanotechnol 2010;5(8):574.

[20] Guadagno L, Raimondo M, Vietri U, Vertuccio L, Barra G, De Vivo B, et al. Effective formulation and processing of nanofilled carbon fiber reinforced composites. RSC Adv 2015;5(8):6033-42.

[21] Guadagno L, Vietri U, Raimondo M, Vertuccio L, Barra G, De Vivo B, et al. Correlation between electrical conductivity and manufacturing processes of nanofilled carbon fiber reinforced composites. Composites Part B 2015;80:7-14.

[22] Guadagno L, Naddeo C, Raimondo M, Barra G, Vertuccio L, Russo S, et al. Influence of carbon nanoparticles/epoxy matrix interaction on mechanical, electrical and transport properties of structural advanced materials. Nanotechnology 2017;28(9):094001.

[23] Vertuccio L, Russo S, Raimondo M, Lafdi K, Guadagno L. Influence of carbon nanofillers on the curing kinetics of epoxy-amine resin. RSC Adv 2015;5(110):90437-50.

[24] Marquardt DW. An algorithm for least-squares estimation of nonlinear parameters. J Soc Ind Appl Math 1963;11(2):431-41.

[25] Maddams W. The scope and limitations of curve fitting. Appl Spectrosc 1980;34(3):245-67.

[26] Guadagno L, Raimondo M, Vertuccio L, Mauro M, Guerra G, Lafdi K, et al. Optimization of graphene-based materials outperforming host epoxy matrices. RSC Adv 2015;5(46):36969-78.

[27] Hermans PH, Weidinger A. On the determination of the crystalline fraction of polyethylenes from X-ray diffraction. Macromol ChemPhys 1961;44(1):24-36.

[28] Tadokoro H. Structure of crystalline polymers: Krieger Pub Co; 1979.

[29] Ju H-M, Huh SH, Choi S-H, Lee H-L. Structures of thermally and chemically reduced graphene. Mater Lett 2010;64(3):357-60.

[30] Kouroupis-Agalou K, Liscio A, Treossi E, Ortolani L, Morandi V, Pugno NM, et al. Fragmentation and exfoliation of 2-dimensional materials: a statistical approach. Nanoscale 2014;6(11):5926-33.

[31] Zhang Q, Yu Y, Yang K, Zhang B, Zhao K, Xiong G, et al. Mechanically robust and electrically conductive graphene-paper/glass-fibers/epoxy composites for stimuli-responsive sensors and Joule heating deicers. Carbon 2017;124:296-307.

[32] Vidano R, Fischbach D, Willis L, Loehr T. Observation of Raman band shifting with excitation wavelength for carbons and graphites. Solid State Commun 1981;39(2):341-4.

[33] Ferrari A, Rodil S, Robertson J. Interpretation of infrared and Raman spectra of amorphous carbon nitrides. Phys Rev B. 2003;67(15):155306.

[34] Jeon I-Y, Shin Y-R, Sohn G-J, Choi H-J, Bae S-Y, Mahmood J, et al. Edge-carboxylated graphene nanosheets via ball milling. Proc Natl Acad Sci 2012;109(15):5588-93.

[35] Childres I, Jauregui LA, Park W, Cao H, Chen YP. Raman spectroscopy of graphene and related materials. New developments in photon and materials research. 2013;1.

[36] Ferrari AC, Meyer J, Scardaci V, Casiraghi C, Lazzeri M, Mauri F, et al. Raman spectrum of graphene and graphene layers. Phys Rev Lett 2006;97(18):187401.

[37] Khanra P, Kuila T, Kim NH, Bae SH, Yu D-s, Lee JH. Simultaneous bio-functionalization and reduction of graphene oxide by baker's yeast. Chem Eng J 2012;183:526-33.

[38] Khan ZU, Kausar A, Ullah H. A review on composite papers of graphene oxide, carbon nanotube, polymer/GO, and polymer/CNT: Processing strategies, properties, and relevance. Polym Plast Technol Eng 2016;55(6):559-81.

[39] Sridhar V, Oh I-K. A coagulation technique for purification of graphene sheets with graphene–reinforced PVA hydrogel as byproduct. J Colloid Interface Sci 2010;348(2):384-7.

[40] Ciambelli P, Sarno M, Gorrasi G, Sannino D, Tortora M, Vittoria V. Preparation and physical properties of carbon nanotubes–PVA nanocomposites. J Macromol Sci B 2005;44(5):779-95.